Vibration-induced assembly of topologically interlocked materials

Aram Bahmani [a], J. William Pro [a], Francois Barthelat [a,b,*]

[a] *Department of Mechanical Engineering, McGill University, Montreal, QC H3A 0C3, Canada*
[b] *Department of Mechanical Engineering, University of Colorado, 427 UCB, 1111 Engineering Dr, Boulder, CO 80309, United States*

ARTICLE INFO

ABSTRACT

Dense architectured, granular, and other material systems based on the assembly of discrete building blocks provide mechanical responses not ordinarily achieved in monolithic materials. The performances of these material systems can be tuned and expanded by simply changing the building block geometry, their packing arrangement, and/or their jamming states. Applications for these material systems have however remained limited, in part because of fabrication challenges and scalability. We explored the vibration-driven assembly method to form periodic arrangements of convex polyhedral building blocks into large-piece free-standing topologically interlocked panels. We used a combination of experiments and discrete elements modeling (DEM) to explore how vibration can be manipulated to steer polyhedral building blocks into one of three possible states: static, assembly, and fluttering and study the governing physics and mechanics underlying these states. The results specified the role of the normalized relative acceleration of mechanical agitation, bouncing, and rotation mechanisms on both phase transitions and crystallization and/or interlocking. The geometry-dependency, re-fragmentation, re-crystallization, and re-configurability of athermal out-of-equilibrium material systems can be understood and optimized based on our findings and provided guidelines in this study.

1. Introduction

Hard convex polyhedral blocks can be assembled and/or fabricated into crystal-like arrangement to create topologically interlocked materials (TIMs) [1–8]. This emerging concept of building block-based architectured materials produces materials with a rich set of tunable mechanisms and properties, based on morphological and interfaces at length scales intermediate between building block size and component size [1–8]. Block-based materials and structures are at the intersection between composite materials, masonry, architectured materials and granular materials, with which they share many similarities: they can temporarily have phase transitions and therefore, they are out-of-thermodynamic equilibrium in their amorphous state while they can be crystallized and stay in a state of equilibrium (the lowest possible potential energy is reached for each building block). In addition, block-based materials and structures provide ample tunable mechanisms, precise compositional and structural gradients, functionalities, and stiff-to-flexible transitions not ordinarily found in monolithic solids [1–10]. The performance of these information-rich materials have been pushed to the extreme by manipulating geometry and/or functionalizing the surface of building blocks resulting in more architectural complexity

[2–6,11,12]. For example, U-shape [13], Z-shape [14], hexapod [15] blocks were used to create tensile strength, but these efforts remain limited by randomness and/or poor packing density of building blocks. The broader application of these complex material systems is also hampered by fabrication challenges; for example, for polyhedral blocks, the most common assembly method is manual [2,4,7,8]. An underused yet potential approach for fabricating these materials is self-assembly which is intrinsically driven by thermal fluctuations at nanoscales and/or colloidal scales [16–19]. Thermal fluctuations, however, do not affect the larger scales (meso- and macro-scales) and athermal systems; therefore, a promising alternative can be mechanical agitating and/or shearing [20–33]. In addition, innovative fabrication methods have been developed for complex composite materials inspired by nacre, bone, or tooth enamel including ice templating [34–36], magnetically assisted slip casting [37], centrifugation [38], and 3D-printing [39]. The vast majority of meso- and macro-scale granular assembly studies have sought the packing and phase transition of spherical grains [9,10, 20–24], and much fewer studies have focused on the polyhedral blocks [25–42], while self-interlocking and/or -crystallization of these geometries has yet been explored particularly at the meso- and macro-scales. Various governing mechanisms underlying packing and temporary phase transitions of granular materials have been explained in the

---

Nomenclature		l	the edge length of square medial section
		N	rotation constant value
A	applied vibration amplitude	S	the area of medial section
a	the edge length of hexagonal medial section	V	the volume of one block
C	rotation constant value	α	interlocking angle
D	the diameter of sphere	Γ	critical relative acceleration
E	elastic modulus	θ	initial misaligned angle of the block
f	applied vibration frequency	ρ	density
g	gravitational acceleration	σ_c	compressive strength
h	the height of blocks	σ_t	tensile strength
$\langle h \rangle$	averaged height of the bouncing sphere	ω	angular velocity
I_{xx}, I_{yy}	normalized out-of-plane moment of inertia		

literature; for instance, the "magnitude" of the mechanical agitation has often been characterized by a single parameter: the critical acceleration normalized by the gravitational acceleration [9,10,43,44]. However, the effective mechanisms involved in self-interlocking and/or -crystallization of polyhedral blocks have yet been established. Vibration-driven assembly has recently been introduced as a potential candidate to crystalize polyhedral building blocks [25,27,41]; however, a comprehensive understanding of the mechanisms governing the vibration-guided assembly of polyhedral blocks is required to use this fabrication method for the large-scale TIMs and other complex block-based architectured material systems [41]. In this work, we examine a vibration-driven assembly method to efficiently fabricate large TIM panels at the millimeter scale using polyhedral building blocks. We decouple the effects of vibration amplitude and frequency on the possible states of the system including interlocking and/or crystallization and temporary phase transitions. We also present discrete element models (DEM) of the assembly, which we use in complement to the experiments to assess and predict the physics and mechanics underlying vibration-driven assembly.

1.1. Geometrical design

To design the individual blocks considered here we used a protocol developed by Dyskin et al. [7,45], where individual blocks are constructed from their medial section, chosen to tessellate the plane (which becomes the medial plane in the TIM panel). We first considered $l \times l$ square medial sections for the individual blocks, which we then extruded to form $l \times l \times h$ square prism (Fig. 1A). Based on this shape, truncated tetrahedra are produced from the square medial section by tilting one opposing pair surfaces of the square prism inward by an angle α, and the other remaining opposite pair surfaces outward by the same angle (Fig. 1A) [2]. We isolated the effect of geometry by fixing $l = 5$ mm and adjusting h from 4.7 mm (square prism) to 5 mm (truncated tetrahedron). In this way, the areal density ($\rho V/S = 1.09$ g/cm^2, ρ is the density, V is the volume of one block, and S is the area of medial section) of both square prism and truncated tetrahedron remains constant. We also consider hexagonal medial sections, which formed hexagonal prisms after extrusion (Fig. 1B). The edge length of hexagonal medial section was set to $a = 3.25$ mm, while the thickness h was adjusted from 4.3 mm (hexagon prism) to 5.3 mm (octahedron) to maintain a constant areal density. The truncated octahedra are created from the hexagonal medial section by tilting six side surfaces of the hexagonal prism: alternating every other surface inward and outward by the same interlocking angle α [2]. For each medial section, α was varied from 0° to 20°, creating truncated tetrahedron and octahedron (Fig. 1A, B). The assembly of these blocks into interlocking structures is shown on Fig. 1C. We focused on these geometries because (i) the effect of different block geometries tessellated from the same medial section on the vibration-driven assembly and crystallization has to yet be explored; (ii) blocks that can interlock are superior to other tessellated building blocks

in generating high-performance mechanical responses for TIMs [2]; (iii) the interlocking of these geometries achieves when they stand on one of their flat faces by which they are stable on the assembly platform (a flat substrate)—a practical advantage for the vibration-driven assembly process. There are other geometries that tessellated by increasing α beyond 20°, which produces the limiting cases of tetrahedron (square medial section) and rhombohedron (hexagonal medial section) (Fig. 1D) [2]. However, in practice these geometries are highly unstable, and the blocks tilted on their side during the experiments.

1.2. Fabrication and experiments

We produced the building blocks described above using a replica casting method with calcium sulfate, using a method described in a previous report [2] which creates dense and homogeneous blocks with uniform geometry and smooth surfaces. We used the strongest type of calcium sulfate plaster (type V from Suprastone, Kerr Dental, Charlotte, NC) with a protocol that maximized density and strength at room temperature [2,46]. The mechanical properties of this calcium sulfate were reported in [2,46] (density $\rho = 2.3$ g/cm^3, Young's modulus $E = 11$ GPa, compressive strength $\sigma_c = 90$ MPa, and tensile strength $\sigma_t = 31$ MPa). The modulus and density of this material provide low resonant frequency response for the building blocks (order of ~1.43 MHz) which was higher than the applied vibration frequency in the assembly process (order of ≤ 1 kHz) [41]. The elastic modulus and the density of the material also govern the time scale of the contact interactions, which we wanted to be much smaller than other characteristic time in the system. Fig. 2A shows the vibration-driven setup that we used for assembly and/or crystallization of the building blocks. We use a polymethylmethacrylate (PMMA) ($E = 2.9$ GPa) assembly platform with edge walls of precise geometry that conform the geometry of the blocks to serve as assembly templates. We centered and glued this assembly platform onto a voice coil, depending on the applied vibration amplitudes and frequencies, we used either a 45 W/60W-RMS/peak or a 120 W/240 W RMS/peak. We mounted this vibration configuration on a 10° tilted platform, where the lowest point of the assembly platform was its corner. With this chosen tilt angle, blocks resting on the platform did not move unless vibration was applied. The applied vibration amplitudes and frequencies were calibrated using a laser vibrometer (Fig. 2A). We used a sinusoidal waveform because it can be generated using a speaker without significant signal overshoot and also additional inertia of the assembly platform. We explored a wide range of vibration amplitudes (1–100 μm with 5 μm intervals) and/or frequencies (10~1000 Hz with 50 Hz intervals) to assess the packing and/or interlocking responses of each polyhedral building blocks in Fig. 1C. Sixty four building blocks were dropped onto the vibrating platform at intervals of ~0.1–~1 s. Fig. 2B shows a schematic of a high-speed camera view that used to monitor the possible mechanisms involved in the vibration-driven assembly process and to measure the final packing factor at the actual steady-state condition (Fig. 2C). Fig. 2B also shows the mobility of the
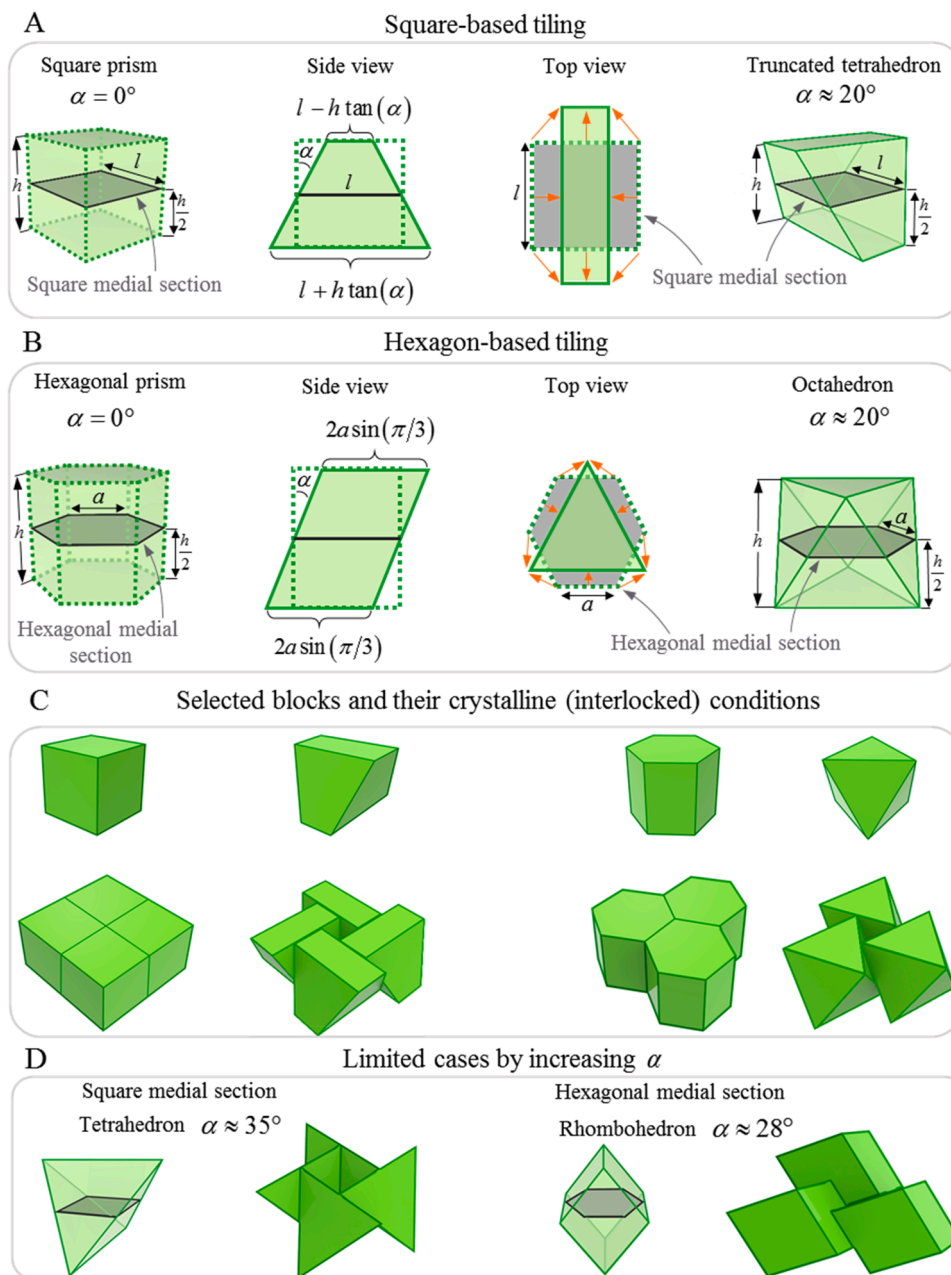
Fig. 1. Overview of four building blocks categorized based on their medial section (A) square-based tiling; (B) hexagon-based tiling: For each category, the tessellation from the basic prism geometry to the truncated version; (C) the crystal and/or interlocked conditions for each geometry; (D) the limited geometries for vibration-driven assembly generated by increasing α in each medial section.

octahedron building blocks toward their minimum potential energy position (the lowest corner of the platform). Once the assembly was complete (that is when the position of the blocks did not change anymore), the packing and/or interlocking efficiency was measured using image analysis, where the domain of building blocks in the binarized images was closely captured by bounding contour (Fig. 2C) using "boundary function" more details for image analysis described in [41]. We defined the steady-state packing factor (PF) as the sum of the projected top surface area for each block divided by the bounding contour area (Fig. 1C), which is outer boundary of the block assembly. For each geometry, we conducted 400 combinations of amplitudes and frequencies and repeated these combinations five times and measured the average packing factor from these repetitions, which in total is 2000 tests. The obtained packing factor was then normalized by the theoretical maximum packing factor for each block geometry. In this way, the

unique packing and interlocking conditions of each geometry can be defined and comparable; for example, normalized packing factor 1 represents perfectly interlocked and/or crystalline for all geometries. The results showed that the normalized packing factor in steady state is independent of the initial position of the dropped block and therefore, the system is memoryless.

We finally interpolated the discrete experimental results to get an assembly map composed of continuous boundaries (Fig. 3). Three main regimes and phase transitions between these regimes were identified for this system based on the dimensionless applied amplitudes and frequencies: A "Static" regime was observed at low vibration amplitudes and/or low frequencies. In this regime the building blocks did not move on the platform due to insufficient applied vibrational energy for overcoming frictional forces, disabling packing factor measurements. An "Assembly" regime was observed at higher vibration amplitudes and/or
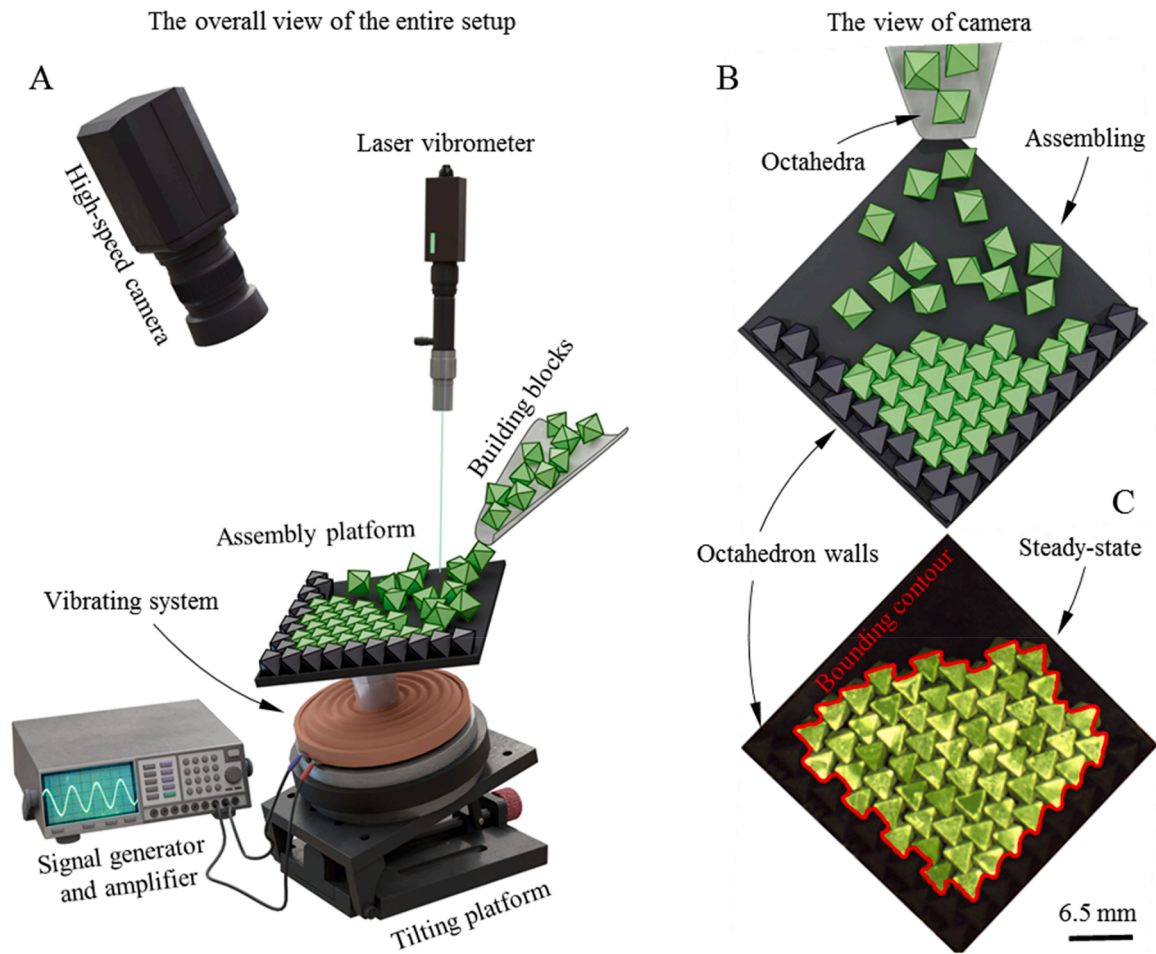
Fig. 2. (A) Schematic of the vibration-driven assembly process integrated with a high-speed camera and laser vibrometer. (B) Polyhedral building blocks are randomly dropped on the tilted assembly platform with block-like walls (template) while it is vibrating. (C) Crystalline (interlocked) packing at steady-state condition measured by image analysis through overlaid bounding contour.

frequencies. In this regime the building blocks bounced and rotated on the platform substrate, enabling movement and the assembly of the blocks into a panel. A steady-state packing factor (PF) could be measured at end of this regime. Finally, a "Fluttering" regime was observed at higher vibration amplitudes and/or frequencies. The building blocks in this regime bounced and overturned constantly in a chaotic manner that prevented packing. Fig. 3 shows these regimes and phases transitions as well as snapshots of the building blocks at each regime based on the dimensionless amplitude $2A/h$ and frequency $f\sqrt{h/2g}$, where A and f are applied vibration amplitude and frequency, h is the height of building blocks, and g is the gravitational acceleration. Fig. 3 shows that each building block geometry has a unique amplitude-vibration range for the assembly regime; however, the variation of packing factor followed a common trend. The packing factor gradually increased by increasing both amplitude and frequency together from static-assembly phase transition boundary toward the assembly-fluttering transition and reached perfectly interlocked and/or crystalline (PF = 1) near this boundary. Square prisms (Fig. 3A) produced the widest assembly regime among other geometries in this study, while hexagonal prism (Fig. 3C) has the largest maximum packing factor region (PF = 1). In addition, increasing α from 0° to 20° in both square- and hexagon-based tiling narrows assembly regimes and maximum packing factor regions (PF = 1); however, octahedron (Fig. 3D) is superior to both square prism and truncated tetrahedron in maximum packing factor region (PF = 1). Truncated tetrahedron (Fig. 3B) has the narrowest assembly regime and maximum packing factor region (PF = 1) with the widest fluttering regime, which reflects that this geometry is

more difficult to assemble. Fig. 3 demonstrates that hexagon-based tiling geometries have the largest maximum packing factor region (PF = 1); therefore, they are easier to perfectly be crystallized and/or interlocked than square-based tilting geometries.

The phase transitions of granular blocks and their steady-state packing due to vibrations have traditionally been predicted based on critical relative acceleration of vibrating system normalized by gravitational acceleration $\Gamma=A\omega^2/g$ ($\omega=2\pi f$ and A is the vibration amplitude) [29,43,44]. Fig. 3 shows the predictions of this model fitted to phase transitions (static-assembly and assembly-fluttering) for each building block geometry. The closest critical acceleration to the static-assembly boundary was at $\Gamma = 3.8$ for square prism and $\Gamma = 4$ for other remaining building blocks. The closest critical acceleration to the assembly-fluttering boundary was at $\Gamma = 21$ for square prism, $\Gamma = 20$ for truncated tetrahedron and hexagon prism, and $\Gamma = 16$ for octahedron. These predictions were closer to hexagon-based tiling geometries than square-based tiling geometries. However, this model did not predict the entire phases transition boundaries for any building block geometries. In addition, these values are obtained from empirical fitting and have no clear physical significance and insights into the mechanics of assembly. For example, the static-assembly and assembly-fluttering transitions are function of the geometry of the building blocks, an effect which is not captured by accelerations only. The assembly process is a complex phenomenon that results from a fine balance between the energy provided by mechanical vibrations, geometry of the blocks, inertia of the blocks and contact interaction including elasticity and friction. Changes in any of these parameters can potentially impact the assembly results,
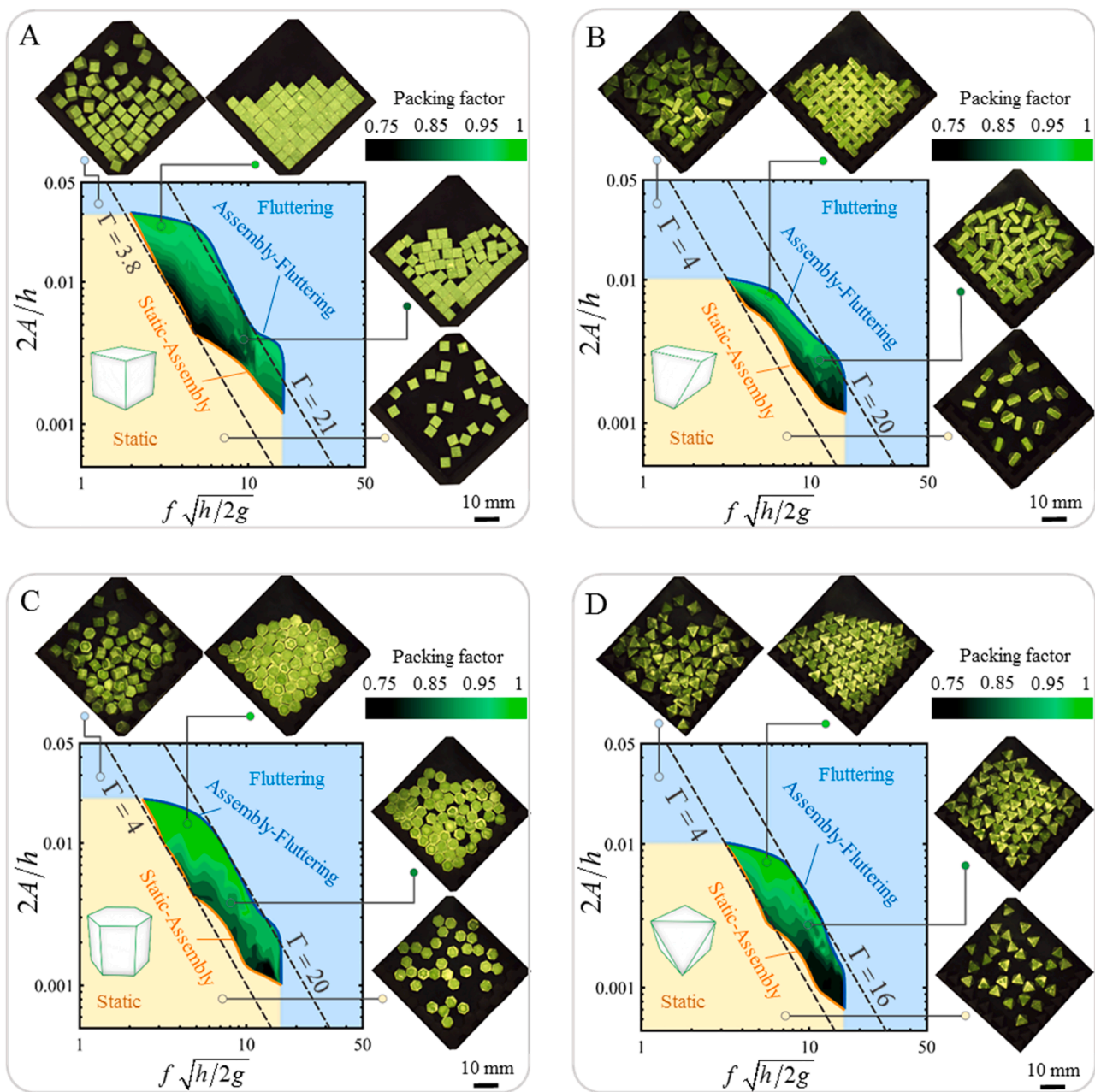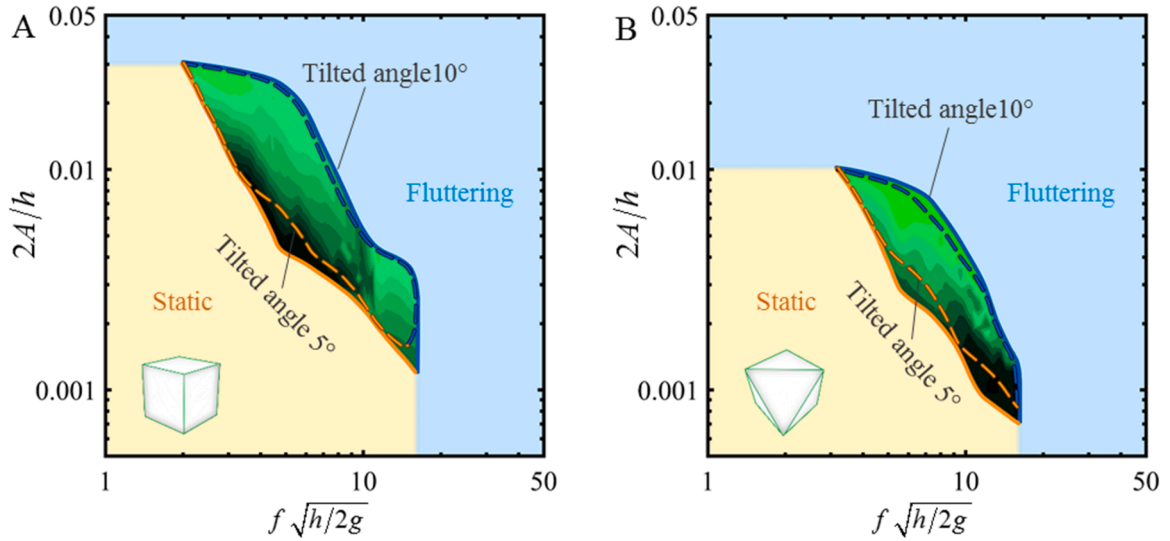
Fig. 3. Experimental assembly phase diagrams demonstrating the various states of the building blocks based on normalized vibration amplitude and frequency (A) square prism; (B) truncated tetrahedron; (C) hexagonal prism; (D) octahedron. These assembly diagrams indicate three main regimes: static, assembly (contoured region representing normalized steady-state packing factor quantified by the colorbar) and fluttering, as well as two phase transitions: static-assembly and assembly-fluttering. The two dash lines exhibit the predictions of fitted critical relative acceleration criterion normalized by gravitational acceleration. For each geometry, the snapshots show the blocks in different regimes: fluttering, high and low packing factor, and static regime.

for example decreasing friction between blocks and the platform would probably shift the static-packing phase transition toward lower amplitudes and frequencies. The tilt angle of the assembly platform can also impact the assembly process. Fig. 4 shows the assembly diagram obtained using 5° and 10° tilt angles, on square prisms and octahedra. The 10° tilt angle slightly extended the assembly regime in terms of both amplitude and frequency range (Fig. 4), because the higher titled angle facilitated the onset of motion in the blocks. Higher angles however led to individual blocks titling on their side, which hindered assembly. The dimensions of the blocks varied within 2–5% around their mean values. It is not clear whether these slight variations in size and shape apparently affected the phase diagram of assembly nor the packing factor of interlocking and/or crystallization."

Fig. 5 shows that meso-scale polyhedral granular building blocks can be self-interlocked and/or -crystallized into macro-scale TIMs using vibration-driven assembly and can be released from assembly platform to be used as a large-piece free-standing stiff architectured panel.

1.3. Discrete element modeling

We used discrete element modeling (DEM) to better understand the phase transition and crystallization (interlocking) of each building block geometry during vibration-driven assembly process. The open-source C++/ Python DEM solver Granoo that we used is particularly developed to model polyhedral granular blocks [47–49]. A contact model that explicitly captures surface roughness was not used here. Instead, we

Fig. 4. Comparisons between experimental assembly phase diagrams for two different assembly platform tilted angles (5 and 10°); (A) square prism; (B) octahedron.

used a linear frictional contact model based on the GJK-EPA algorithm [43]. This algorithm detects collision and compute penetration distance between colliding blocks, from which a contact force is computed. We used a linear contact model where the contact is governed by a single contact stiffness, which is an acceptable approximation for intermittent contacts (this approximation of the contact also led to good agreements with the experiments). The experimental physical dimensions and properties were directly duplicated into the DEM simulations. The block-on-block static and dynamic friction coefficients were 0.4 and 0.33, and the block-on-platform static and dynamic friction coefficients were 0.38 and 0.27. The block-on-block contact stiffnesses was set at 150 kN/mm and the block-on-platform contact stiffnesses was set at 700 kN/mm. The block-on-block and block-on-platform coefficients of restitution were 0.3 and 0.4. These values and more details for experimental measurement of these properties are described in [41]. These DEM simulations were first compared with the experimental results for validation. We non-uniformly dispersed and randomly dropped 64 building blocks onto the vibrating tilted (10°) platform subjected to gravitational acceleration and vertical sinusoidal displacement during 100 s which was adequate time to capture the response of the system for any applied vibration amplitudes and/or frequencies for each building blocks geometry. Fig. 6 shows the DEM-generated assembly phase diagrams based on the dimensionless vibration amplitude and frequency for different building block geometries, together with snapshots at each of the regimes. The DEM simulations duplicated the phase transition contours from the experiments quite accurately. The packing factor predicted by the DEM simulation were repeatable and independent of the initial dropping position of blocks and consistent with experiments. We repeated each simulation (for each applied vibration amplitude and/or frequency) five times with randomly dispersed block positions, the packing factor was memoryless, and its deviation from the mean did not exceed 10% for each building block geometry. In agreement with the experiments, the maximum packing factor region (PF = 1) in DEM was also achieved by high vibration amplitudes and/or low frequencies for each building block geometry. The DEM-generated packing factor also is increased from the static-assembly to the assembly-fluttering phase transition boundary. We used the same method as the experiments to interpolate continuous domains from the discrete modeling results to get an assembly map shown on Fig. 6. The square prism (Fig. 6A) has the largest assembly regime; the truncated tetrahedron (Fig. 6B) has the smallest assembly regime and largest fluttering regime. DEM also properly captured the effects of increasing α from 0° to 20° in both square- and hexagon-based tiling, creating smaller assembly regimes

and maximum packing factor regions, as well as wider fluttering regimes. The critical relative acceleration criterion did not fit experimental transition well nor DEM predictions. In the following section, we use DEM to capture the rotation and bouncing mechanisms of individual blocks to create a fundamental understanding of the assembly process.

2. Mechanisms of individual blocks

2.1. Bouncing

Our observations (high-speed camera imaging) during the vibration-driven assembly process exhibit that each building block may have an effective bouncing mechanism enabling mobility and thus overcoming the friction of blocks with the assembly platform. Predicting the bounce height of an individual polyhedral building block bouncing on a vibrating flat substrate is a seemingly simple problem; however, it is a complex nonlinear phenomenon that can enter into a chaotic fashion because of bouncing itself and variations in bouncing direction due to geometrical angular features [41,50–52]. Therefore, a simple and generalizable geometry is required to assess the bouncing mechanism of polyhedral blocks by eliminating geometrical angular features and possible bouncing directions. A single sphere bouncing on a harmonic vibrating rigid platform was modeled in the DEM to explore the effect of experimental physical and vibrational parameters on the bouncing mechanism [41]. These DEM results were used to measure the non-dimensional time-averaged height of the bouncing sphere based on the normalized applied vibration amplitude and frequency. The obtained equations for average bounce height given by [41]:

$$\frac{\langle h \rangle}{D} = 7.5 \left(\frac{2A}{D} \right)^2 \left(f \sqrt{\frac{D}{2g}} \right)^{2.1} \tag{1}$$

where D is the diameter of the sphere; $\langle h \rangle$ is averaged height of the bouncing sphere. This obtained equation also demonstrates that vibration amplitudes and frequencies have almost the same powers, and therefore their contribution must be taken into account separately in the context of a vibration-driven assembly [23,24,41].

2.2. Rotation

In addition to bouncing, rotation also promotes interactions among polyhedral building blocks and is another effective block-based mechanism observed in the vibration-driven crystallization and/or inter-
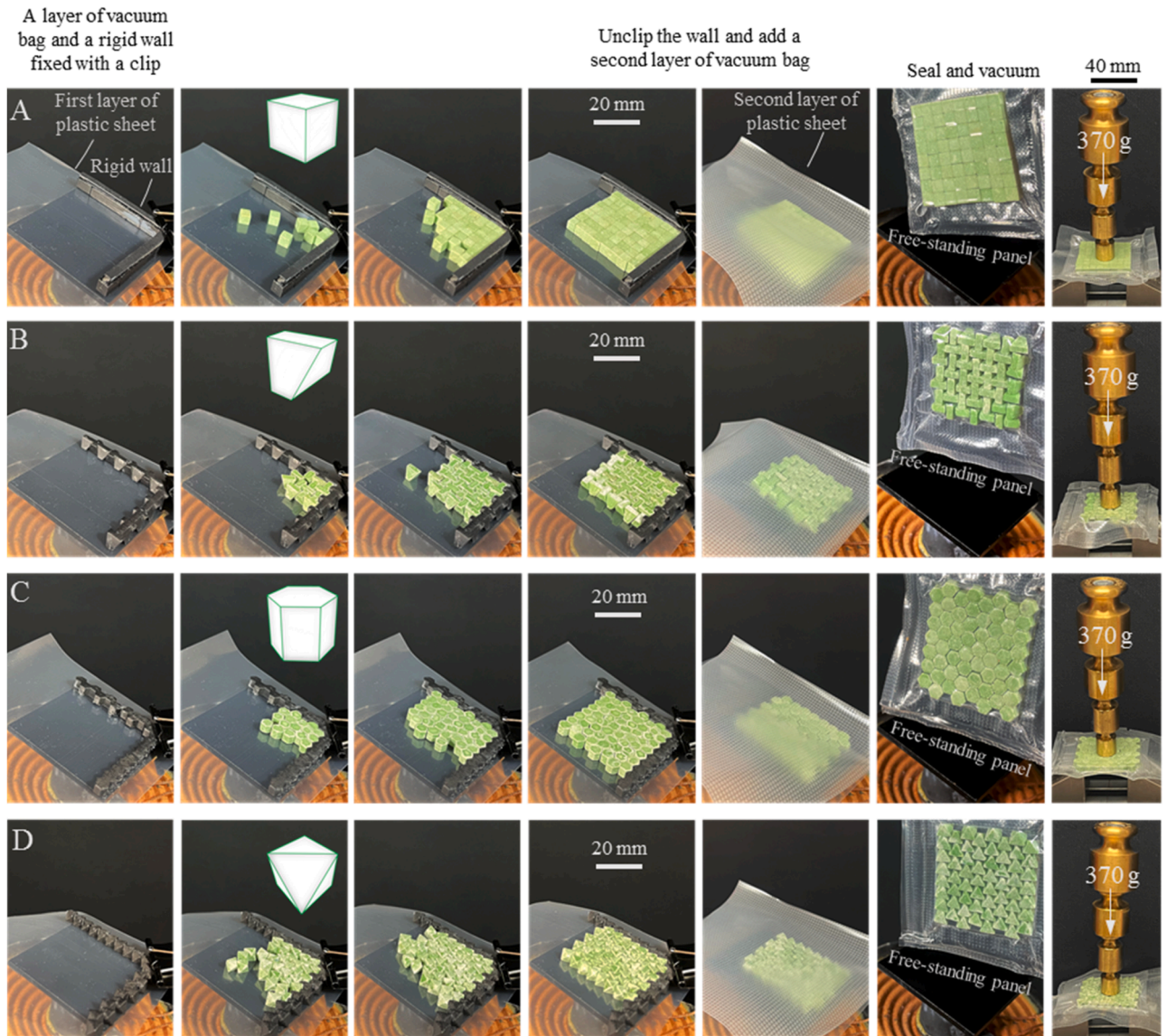
Fig. 5. The self-interlocking and/or crystallization process of (A) square prism, (B) truncated tetraheron, (C) hexagon prism, and (D) octahedron building blocks into dense free-standing TIM monolayer as a large piece material and/or structure.

locking process, steering building blocks toward the available vacancies [41]. This mechanism is not well understood for polyhedral building blocks; therefore, we used a single-block DEM simulation for each geometry with the same dimensions and physical properties as in experiments. Our objective was to capture the conditions in which a single-block rotates from a misaligned static equilibrium condition to perfectly align position (producing interlocking and/or crystallization) or transition from rotation to chaotic fashion (fluttering). We used this single-block DEM simulation to explore the rotation-based mechanism of each building block geometry based on the initial misaligned angle, applied vibration amplitudes and/or frequencies. The single block that we placed at the corner of a tilted (10°) rigid platform with block-like walls (the same shape as the blocks) has an initial misaligned angle (θ) (Fig. 7). This configuration initially was subjected to only gravity, and the rotated block was settled by contact (friction) with block-like walls in a static equilibrium condition. The platform was then subjected to a vertical sinusoidal displacement for 5 s which was adequate time to capture the rotation response of building block for any applied vibration amplitudes and/or frequencies. This model replicates a local configuration where a building block interacts with nearest neighbors and/or the assembly platform and will be interlocked and/or crystalline

when it rotates from misaligned position. The polar plots in Fig. 7 show the radial phase diagram for each building block geometry indicating the state of single block (static, rotating to assembly or fluttering) based on Γ and the initial misaligned angle of the block (θ). These polar plots exhibit that the rotation of each building block is independent of the medial section geometry because each block has a unique rotation symmetry regardless of their geometry transformation from the same medial section (square prism to truncated tetrahedron and hexagonal prism to octahedron). For all building block geometries, the misaligned angle θ governs the static-rotating transition, while Γ governs the rotating-fluttering boundary. The results can be fitted with expression:

$$\frac{A}{h} = C\left(f\sqrt{\frac{h}{2g}}\right)^n \tag{2}$$

A general form of power Eq. (2) can be fitted to radial phase transitions based on the applied vibration amplitudes and frequencies for all building block geometries. The constant values (C and n) for each building block geometry and phase transition are indicated in Fig. A1.
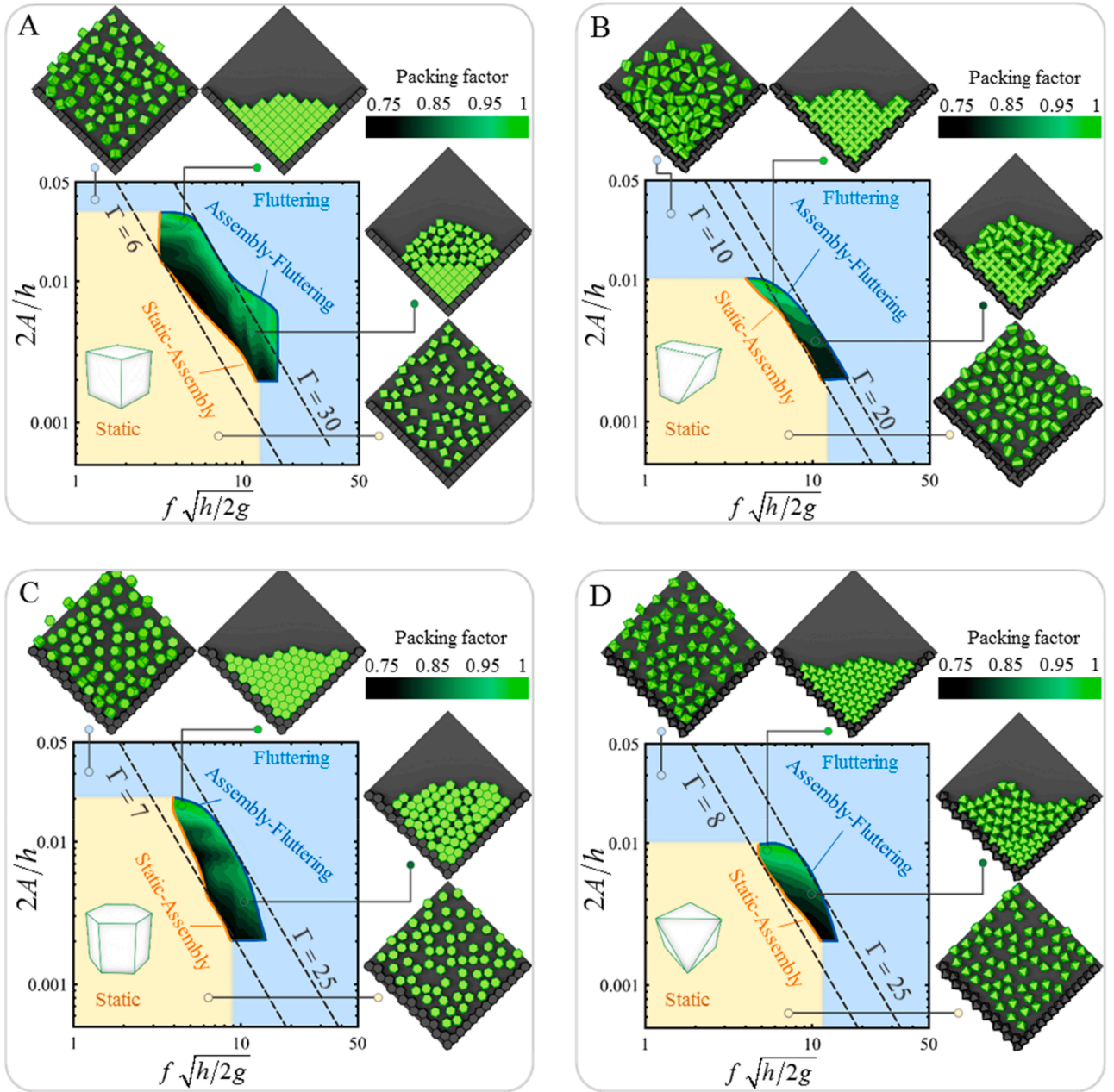
Fig. 6. DEM-generated phase diagrams indicating the various states of the building blocks based on normalized vibration amplitude and frequency (A) square prism; (B) truncated tetrahedron; (C) hexagonal prism; (D) octahedron. These assembly phase diagrams show three main regimes: static, assembly and fluttering. as well as two phase transitions: static-assembly and assembly-fluttering. The contours quantified by the colorbar represent the variation of the steady-state normalized average packing factor, which was measured by the bounding contour the same as experiments. The two dash lines exhibit the predictions of fitted critical relative acceleration criterion normalized by gravitational acceleration. For each geometry, the snapshots show the blocks in different regimes: fluttering, high and low packing factor, and static regime.

2.3. Assembly phase diagram assessments with individual block mechanics

In this section, we assess the effect of block-based mechanisms on the phase transitions and compare these models with the critical relative acceleration criterion. We also seek effective regimes, phase transitions, and geometrical dynamic characteristics, making a geometry an easier building block for vibration-driven assembly than another geometry. In addition to the critical relative acceleration criterion, the two DEM-generated models presented above (bounce height and rotation) were superimposed to the experimental assembly phase diagrams indicated in Fig. 3 and shown in Fig. 8. The critical relative acceleration criterion

predicts the transition boundaries of hexagon-based tiling geometries (Fig. 8C, D) more precisely than square-based tiling geometries (Fig. 8A, B). This empirical model is based on the vibrating system, and therefore, it does not consider the building block geometry and/or the mechanisms involved in phase transitions. In contrast to the critical relative acceleration criterion, the bounce height model has advantages to be based on the phenomenological model of building block mechanism; however, this model also has a fitting parameter that varies by changing building block geometry. Fig. 8 exhibits that the bounce height model was more successful in predicting the phase transitions of square-based tiling geometries (Fig. 8A, B) than hexagon-based tiling geometries (Fig. 8C, D). The rotation model is a purely phenomenological based on the actual
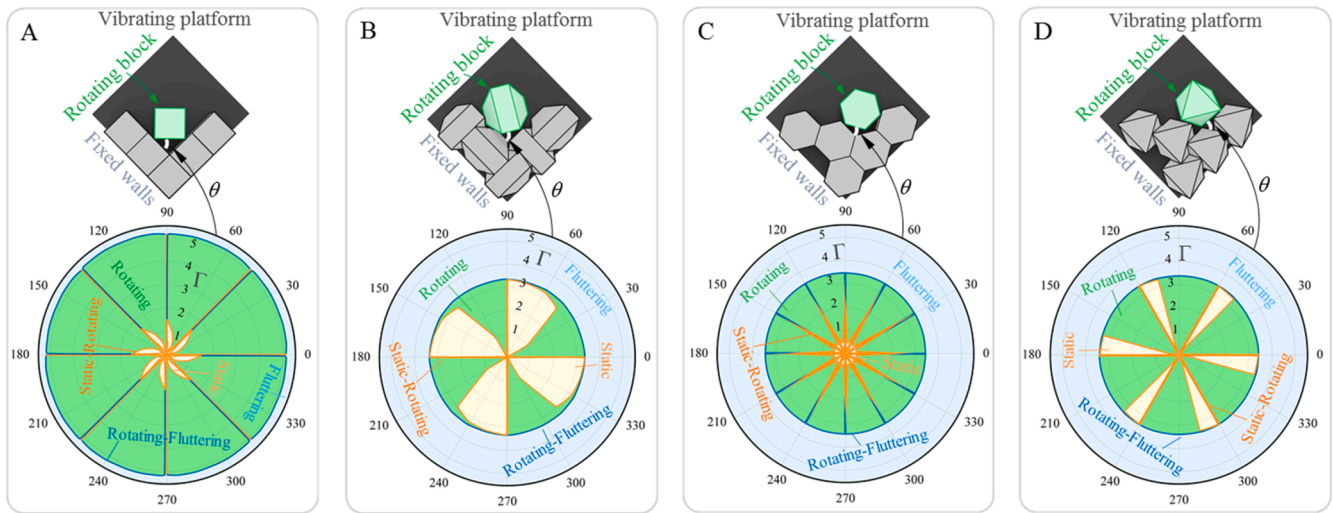
Fig. 7. Schematics of the single-block DEM models rotating due to the vibration of the tilted rigid platform. Radial phase diagrams computed by these single-block DEM models as function of dimensionless critical relative acceleration (Γ) and initial misaligned angle (θ) for each building block. (A) Square prism; (B) truncated tetrahedron; (C) hexagonal prism; (D) octahedron.

geometry of building block and its rotation mechanism; therefore, there is no fitting parameter and/or dependency on building block geometry in this model. The overall trends of transition boundaries were nearly captured while this model captures the high packing factor regions reasonably well for all building block geometries implying that the rotation mechanism may not utterly be involved in the phase transitions, but it is one of the key mechanisms in the assembly regime. In addition, the overlap between rotation and bounce height model in high packing factor regions for all building geometries, suggests that both rotation and bouncing are the key mechanisms for vibration-driven assembly.

A building block can be assembled easier than another one with a different geometry when it has a wider assembly regime with a broader range of vibration amplitudes and frequencies in the assembly phase diagram. Fig. 9A shows that the static-assembly boundary is nearly the same for building block geometries used in this study; however, their assembly-fluttering boundary is different. For example, the static regime for truncated tetrahedron is the smallest due to its largest fluttering regime. Therefore, a building block with the wider fluttering regime is more difficult to be self-interlocked and/or -crystallized due to its instability during assembly process (truncated tetrahedron and octahedron). In a perfectly interlocked packing arrangement (PF = 1), finished assemblies of truncated tetrahedra and of octahedra appeared to be more stable because of geometrical interlocking. However, these two geometries are also less stable during the assembly process because of their dynamic characteristics and also their narrow PF = 1 region in terms of amplitude and frequency range (Figs. 3 and 8). From dropping point to steady-state condition, we showed that building blocks might bounce and/or rotate to reach the platform wall or other blocks or perfectly be crystalline and/or interlocked. During this process, a geometry like truncated tetrahedron or octahedron is more unstable than a square and hexagonal prism due to their dynamic characteristics and geometrical angular features, which include the moment of inertia. We showed that bouncing has an additional role in assembly-fluttering transition (Fig. 8), and due to the angular features of each building block geometry, the out-of-plane moment of inertia can be more effective in instability of a building block than rotation and in-plane moment of inertia (I_{zz}). We therefore explored the area of PF = 1 regions (Fig. 3) for each building block as function of the normalized out-of-plane moment of inertia (I_{xx} and I_{yy}) (Fig. 9B). The lower the out-of-plane moment of inertia, the larger the maximum packing factor region (PF = 1) in terms of amplitude and frequency range, implying that perfectly interlocked assemblies (PF = 1) by hexagon-based geometries can be

achieved in a broader range of amplitude and frequency due to their lower out-of-plane moment of inertia compared to square-based geometries (higher out-of-plane moment of inertia). Figs. 9B and 8 also imply that by increasing the out-of-plane moment of inertia, the block-based models are further needed to capture different states of the phases diagram, while the critical relative acceleration model is more prices for geometries with the lower out-of-plane moment of inertia.

3. Summary

Our main findings can be summarized as follows:

- Different polyhedral granular building blocks can be self-crystallized and/or interlocked into topologically interlocked materials (TIMs) and immediately be used as structures.
- The phase diagram of the system was established using experiments and DEM simulations. Static, assembly, and fluttering regimes and their phase transition boundaries were identified. For all block geometries, the optimum packing occurred near the assembly-fluttering transition.
- The assembly phase diagram showed that the crystallized and/or interlocked polyhedral granular building blocks can be re-fragmented by the fluttering regime and then again be re-fabricated by the assembly regime. The fluttering (instability) regime was also effective in reducing the range of assembly regime; a building block geometry with the wider fluttering regime is more difficult to be self-interlocked and/or -crystallized.
- The basic geometries of square and hexagon medial sections (square and hexagonal prism) benefit from wider assembly regimes compared with their truncated versions (truncated tetrahedron and octahedron). While hexagon-based tiling geometries (hexagonal prisms and octahedron) benefits from wider maximum packing factor regions (perfectly interlocked and/or crystalline) compared with the square-based tiling geometries (square prism and truncated tetrahedron).
- Out-of-plane moment of inertial was an effective dynamic characteristic and geometry angular feature on the perfectly interlocked and/or crystalline of building blocks. Geometries with lower out-of-plane moment of inertia had wider maximum packing factor regions.
- Each building block geometry had a distinct static-assembly and assembly-fluttering phase transition. Both boundaries for hexagon-based tiling geometries were nearly correlated with the critical
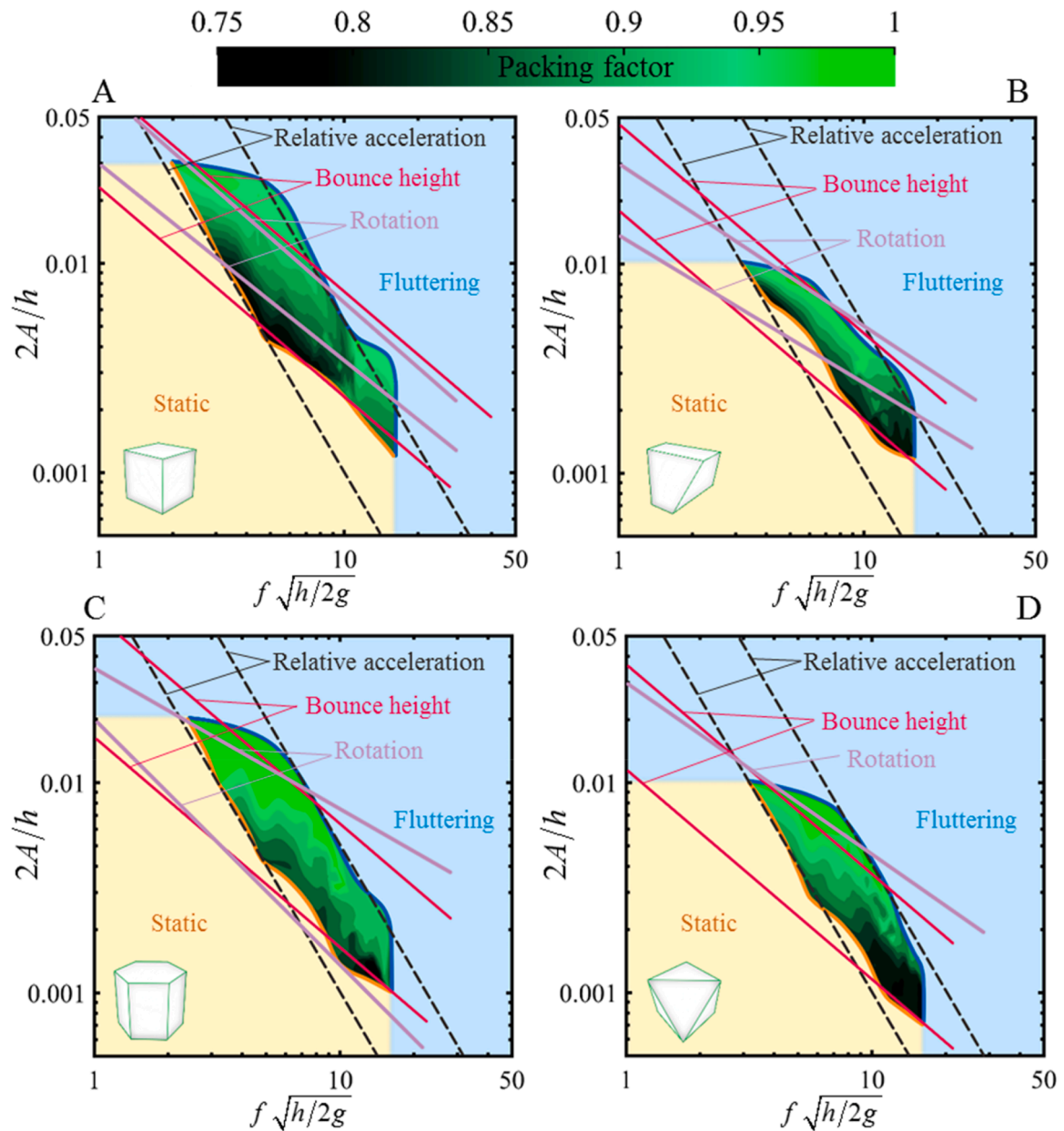
Fig. 8. Comparison between experimental phase transition boundaries (i.e., static-assembly and assembly -fluttering) and assembly regime with critical relative acceleration, bounce height, and rotation models. (A) Square prism; (B) truncated tetrahedron; (C) hexagonal prism; (D) octahedron.

relative acceleration criterion. However, this criterion was not entirely successful for the phase transitions of square-based tiling geometries; a part of these boundaries were correlated with the bounce height and rotation model. The critical relative acceleration was an inadequate parameter to determine the mechanical agitation during vibration-driven assembly of polyhedral granular building blocks. The role of vibration amplitude and frequency must be characterized separately.

- For all building block geometries, the onset of rotation and fluttering was captured by the single-block rotation model, which was purely phenomenological and reasonably correlated well with the phase transition boundaries and maximum packing factor regions.

4. Conclusions

In this study, we assembled stiff square- and hexagon-based polyhedral building blocks into free-standing topologically interlocked and/ hedral building blocks into free-standing topologically interlocked and/

or crystalline monolayers by combining vibration and gravity. We identified three regimes and two-phase transitions for the assembly phase diagram of each building block geometry experimentally and numerically. We generated DEM models to duplicate the experiments and complemented these simulations with single-block DEM models to study the effective mechanisms involved in the assembly and phase transitions of each polyhedral building block geometry.

The physics and mechanics underlying the shape-dependency of athermal out-of-equilibrium material systems can be studied in meso- and macro-scale using the vibration-driven assembly method presented in this study. This method can also be an efficient and promising pathway for self-crystallization and/or -interlocking of polyhedral granular building blocks in different length scales. It can offer new high-potential routes enabling scalable, rapid, and low-energy fabrication method for block-based architectured materials and/or structures in different environments and atmospheres—topologically interlocked materials (TIMs) was a prominent example in this study [1–8]. The
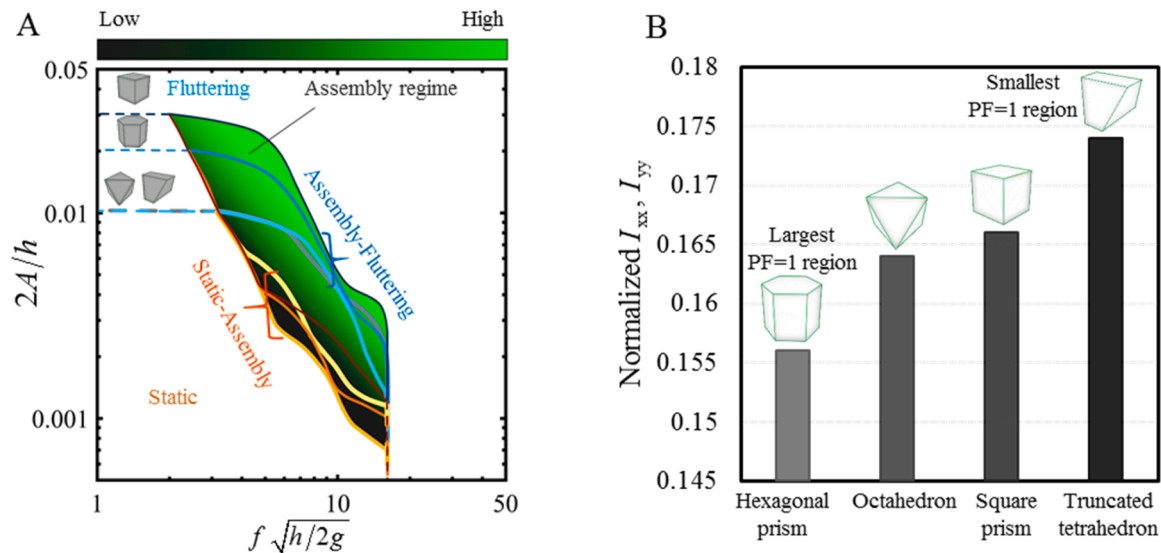
Fig. 9. (A) Comparisons of assembly phase diagrams for four building block geometries; (B) normalized out-of-plane moment of inertia (I_{xx} and I_{yy}) for each geometry verse their maximum packing factor regions (PF = 1).
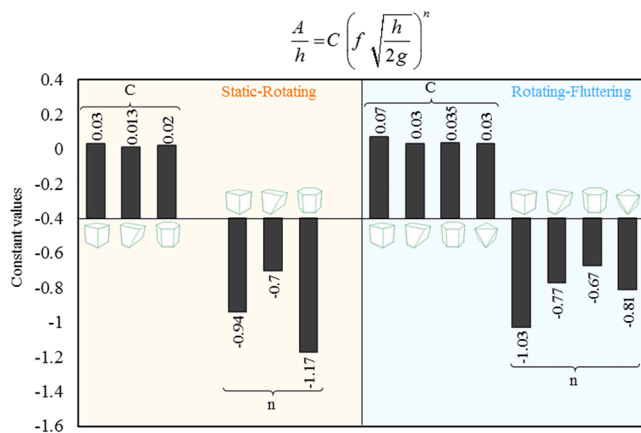
Fig. A1. The constant values of the rotation model for each building block geometry and phase transitions.

assembly method in this study can be used to frequently re-fragment and then again re-fabricate versatile anisotropic and/or hybrid TIM transformable and freeform structures, components, and armors. The assembly method is very robust, especially if a "crystallization front" is created and maintained during assembly by controlling the feeding rate of the blocks onto the assembly platform. In this condition, it would be possible to scale the process to many more building blocks using a larger assembly platform. The vibration-driven method in this study can also have biomedical applications including bone regeneration and healing and manipulating blood clot properties (both projects are currently under investigation). In addition, it can be used to form and assess decentralized and reconfigurable robots made by granular building blocks [53–58]. The principal mechanisms and findings in this study can also be used for other wave-based agitation methods for granular materials such as levitation [20,28,59]. We did not study the effect of different waveforms (signal shapes) and also large size and shape variations. These two parameters need to systematically be studied in future studies.

CRediT authorship contribution statement

Aram Bahmani: Conceptualization, Methodology, Investigation,

Visualization, Writing – original draft, Writing – review & editing. **J. William Pro:** Methodology, Investigation, Writing – review & editing. **Francois Barthelat:** Conceptualization, Methodology, Investigation, Visualization, Supervision, Writing – review & editing.

Declaration of Competing Interest

The authors declare that they have no known competing financial interests or personal relationships that could have appeared to influence the work reported in this paper.

Acknowledgments

Supplementary materials

Supplementary material associated with this article can be found, in the online version, at doi:10.1016/j.apmt.2022.101601.

Appendix

Fig. A1 indicates the constant values for the rotation model. These values are different for each building block geometry and phase transition boundaries (static-rotating and rotating-fluttering).

References

[1] F. Barthelat, Architectured materials in engineering and biology: fabrication, structure, mechanics and performance, Int. Mater. Rev. 60 (2015) 413–430.
[2] M. Mirkhalaf, T. Zhou, F. Barthelat, Simultaneous improvements of strength and toughness in topologically interlocked ceramics, Proc. Natl. Acad. Sci. 115 (2018) 9128–9133.
[3] Y. Wang, L. Li, D. Hofmann, J.E. Andrade, C. Daraio, Structured fabrics with tunable mechanical properties, Nature 596 (2021) 238–243.
[4] T. Siegmund, F. Barthelat, R. Cipra, E. Habtour, J. Riddick, Manufacture and mechanics of topologically interlocked material assemblies, Appl. Mech. Rev. 68 (2016) 0408031–04080315.
[5] K. Mahoney, T. Siegmund, Mechanics of tubes composed of interlocking building blocks, Int. J. Eng. Sci. 174 (2022), 103654.

[6] D.Y. Kim, T. Siegmund, Mechanics and design of topologically interlocked irregular quadrilateral tessellations, Mater. Des. 212 (2021), 110155.

[7] A.V. Dyskin, Y. Estrin, A.J. Kanel-Belov, E. Pasternak, Toughening by fragmentation — how topology helps, Adv. Eng. Mater. 3 (2001) 885–888.

[8] M. Mirkhalaf, H. Zreiqat, Fabrication and mechanics of bioinspired materials with dense architectures: current status and future perspectives, JOM 72 (2020) 1458–1476.

[9] H.M. Jaeger, Celebrating soft matter's 10th anniversary: toward jamming by design, Soft Matter 11 (1) (2015) 12–27.

[10] P. Richard, M. Nicodemi, R. Delannay, P. Ribiere, D. Bideau, Slow relaxation and compaction of granular systems, Nat. Mater. 4 (2) (2005) 121–128.

[11] A.S. Dalaq, F. Barthelat, Manipulating the geometry of architectured beams for maximum toughness and strength, Mater. Des. 194 (2020), 108889.

[12] L. Djumas, G.P. Simon, Y. Estrin, A. Molotnikov, Deformation mechanics of non-planar topologically interlocked assemblies with structural hierarchy and varying geometry, Sci. Rep. 7 (2017) 1–11.

[13] N. Gravish, S.V. Franklin, D.L. Hu, D.I. Goldman, Entangled granular media, Phys. Rev. Lett. 108 (2012), 208001.

[14] K.A. Murphy, N. Reiser, D. Choksy, C.E. Singer, H.M. Jaeger, Freestanding loadbearing structures with Z-shaped particles, Granul. Matter 18 (2016) 26.

[15] J. Barés, Y. Zhao, M. Renouf, K. Dierichs, R. Behringer, Structure of hexapod 3d packings: understanding the global stability from the local organization, in: Proceedings of the EPJ Web of Conferences 140, EDP Sciences, 2017, p. 06021.

[16] V.N. Manoharan, Colloidal matter: packing, geometry, and entropy, Science (2015) 349.

[17] A.R. Chandrasekaran, R. Zhuo, A 'tile' tale: hierarchical self-assembly of DNA lattices, Appl. Mater. Today 2 (2016) 7–16.

[18] J. Li, L. Li, J. Zhou, Z. Zhou, X.L. Wu, L. Wang, Q. Yao, 3D printed dual-functional biomaterial with self-assembly micro-nano surface and enriched nano argentum for antibacterial and bone regeneration, Appl. Mater. Today 17 (2019) 206–215.

[19] D.J. Kraft, R. Ni, F. Smallenburg, M. Hermes, K. Yoon, D.A. Weitz, W.K. Kegel, Surface roughness directed self-assembly of patchy particles into colloidal micelles, Proc. Natl. Acad. Sci. 109 (2012) 10787–10792.

[20] M.X. Lim, A. Souslov, V. Vitelli, H.M. Jaeger, Cluster formation by acoustic forces and active fluctuations in levitated granular matter, Nat. Phys. 15 (5) (2019) 460–464.

[21] X.Z. An, R.Y. Yang, K.J. Dong, R.P. Zou, A.B. Yu, Micromechanical simulation and analysis of one-dimensional vibratory sphere packing, Phys. Rev. Lett. 95 (2005), 205502.

[22] P. Philippe, D. Bideau, Granular medium under vertical tapping: change of compaction and convection dynamics around the liftoff threshold, Phys. Rev. Lett. 91 (2003), 104302.

[23] R. Amirifar, K. Dong, Q. Zeng, X. An, Self-assembly of granular spheres under one-dimensional vibration, Soft Matter 14 (2018) 9856–9869.

[24] R. Amirifar, K. Dong, Q. Zeng, X. An, Bimodal self-assembly of granular spheres under vertical vibration, Soft Matter 15 (2019) 5933–5944.

[25] F. López-González, A.M. Herrera-González, F. Donado, Study of the transition from amorphous to crystalline phase in a granular system under shearing and vibration, Phys. A Stat. Mech. Appl. 590 (2022), 126756.

[26] J. Baker, A. Kudrolli, Maximum and minimum stable random packings of platonic solids, Phys. Rev. E 82 (2010), 061304.

[27] M. Götz, T. Fey, P. Greil, Vibration assisted self-assembly processing of ceramic-based composites with modular meta-structure, J. Am. Ceram. Soc. 95 (2012) 95–101.

[28] M.X. Lim, K.A. Murphy, H.M. Jaeger, Edges control clustering in levitated granular matter, Granul. Matter 21 (2019) 77.

[29] M. Neudecker, S. Ulrich, S. Herminghaus, M. Schröter, Jammed frictional tetrahedra are hyperstatic, Phys. Rev. Lett. 111 (2013), 028001.

[30] K. Asencio, M. Acevedo, I. Zuriguel, D. Maza, Experimental study of ordering of hard cubes by shearing, Phys. Rev. Lett. 119 (2017), 228002.

[31] M. Ramaioli, L. Pournin, T.M. Liebling, Vertical ordering of rods under vertical vibration, Phys. Rev. E 76 (2007), 021304.

[32] A. Jaoshvili, A. Esakia, M. Porrati, P.M. Chaikin, Experiments on the random packing of tetrahedral dice, Phys. Rev. Lett. 104 (2010), 185501.

[33] X. Li, K.M. Lim, W. Zhai, A novel class of bioinspired composite via ultrasound-assisted directed self-assembly digital light 3D printing, Appl. Mater. Today 26 (2022), 101388.

[34] H. Zhao, S. Liu, Y. Wei, Y. Yue, M. Gao, Y. Li, L. Jiang, Multiscale engineered artificial tooth enamel, Science 375 (6580) (2022) 551–556.

[35] H. Zhao, Y. Yue, L. Guo, J. Wu, Y. Zhang, X. Li, X. Han, Cloning nacre's 3D interlocking skeleton in engineering composites to achieve exceptional mechanical properties, Adv. Mater. 28 (25) (2016) 5099–5105.

[36] F. Bouville, E. Maire, S. Meille, B. Van de Moortèle, A.J. Stevenson, S. Deville, Strong, tough and stiff bioinspired ceramics from brittle constituents, Nat. Mater. 13 (5) (2014) 508–514.

[37] H. Le Ferrand, F. Bouville, T.P. Niebel, A.R. Studart, Magnetically assisted slip casting of bioinspired heterogeneous composites, Nat. Mater. 14 (11) (2015) 1172–1179.

[38] A. Amini, A. Khavari, F. Barthelat, A.J. Ehrlicher, Centrifugation and index matching yield a strong and transparent bioinspired nacreous composite, Science 373 (6560) (2021) 1229–1234.

[39] A.R. Studart, Additive manufacturing of biologically-inspired materials, Chem. Soc. Rev. 45 (2016) 359–376.

[40] S.M.M. Valashani, C.J. Barrett, F. Barthelat, Self-assembly of microscopic tablets within polymeric thin films: a possible pathway towards new hybrid materials, RSC Adv. 5 (2015) 4780–4787.

[41] A. Bahmani, J.W. Pro, F. Hannard, F. Barthelat, Vibration-driven fabrication of dense architectured panels, Matter 5 (3) (2022) 899–910.

[42] C. Zhou, S. Liang, Y. Li, J. Li, H. Chen, Microfluidic assembly of microblocks into interlocked structures for enhanced strength and toughness, ACS Appl. Mater. Interfaces (2022).

[43] E.R. Nowak, J.B. Knight, E. Ben-Naim, H.M. Jaeger, S.R. Nagel, Density fluctuations in vibrated granular materials, Phys. Rev. E 57 (1998) 1971–1982.

[44] J.B. Knight, C.G. Fandrich, C.N. Lau, H.M. Jaeger, S.R. Nagel, Density relaxation in a vibrated granular material, Phys. Rev. E 51 (1995) 3957.

[45] Y. Estrin, Y. Bréchet, J. Dunlop, P. Fratzl, Architectured Materials in Nature and Engineering: Archimats, 282, Springer, 2019.

[46] S. Cavelier, S.A. Mirmohammadi, F. Barthelat, Titanium mesh-reinforced calcium sulfate for structural bone grafts, J. Mech. Behav. Biomed. Mater. 118 (2021), 104461.

[47] D. André, J.L. Charles, I. Iordanoff, J. Néauport, The GranOO workbench, a new tool for developing discrete element simulations, and its application to tribological problems, Adv. Eng. Softw. 74 (2014) 40–48.

[48] D. André, J.L. Charles, I. Iordanoff, 3D Discrete Element Workbench For Highly Dynamic Thermo-mechanical Analysis: GranOO, John Wiley & Sons, 2015.

[49] D. André, J. Girardot, C. Hubert, A novel DEM approach for modeling brittle elastic media based on distinct lattice spring model, Comput. Methods Appl. Mech. Eng. 350 (2019) 100–122.

[50] J.J. Barroso, M.V. Carneiro, E.E. Macau, Bouncing ball problem: stability of the periodic modes, Phys. Rev. E 79 (2009), 026206.

[51] R.I. Leine, T.F. Heimsch, Global uniform symptotic attractive stability of the non-autonomous bouncing ball system, Phys. D Nonlinear Phenom. 241 (2012) 2029–2041.

[52] Z.H. Jiang, Z.J. Liang, A.C. Wu, R.H. Zheng, Effect of collision duration on the chaotic dynamics of a ball bouncing on a vertically vibrating plate, Phys. A Stat. Mech. Appl. 494 (2018) 380–388.

[53] B. Saintyves, M. Spenko, H. Jaeger, Granulobot: grom granular matter to self-assembling and reconfigurable robotics, Bull. Am. Phys. Soc., 2022.

[54] C.J. Zimmermann, T. Schraeder, B. Reynolds, E.M. DeBoer, K.B. Neeves, D. W. Marr, Delivery and actuation of aerosolized microbots, Nano Sel. (2022).

[55] W. Wang, J. Giltinan, S. Zakharchenko, M. Sitti, Dynamic and programmable self-assembly of micro-rafts at the air-water interface, Sci. Adv. 3 (5) (2017), e1602522.

[56] R. Niu, C.X. Du, E. Esposito, J. Ng, M.P. Brenner, P.L. McEuen, I. Cohen, Magnetic handshake materials as a scale-invariant platform for programmed self-assembly, Proc. Natl. Acad. Sci. 116 (49) (2019) 24402–24407.

[57] M.Z. Miskin, A.J. Cortese, K. Dorsey, E.P. Esposito, M.F. Reynolds, Q. Liu, I. Cohen, Electronically integrated, mass-manufactured, microscopic robots, Nature 584 (7822) (2020) 557–561.

[58] G. Gardi, S. Ceron, W. Wang, K. Petersen, M. Sitti, Microrobot collectives with reconfigurable morphologies, behaviors, and functions, Nat. Commun. 13 (1) (2022) 1–14.

[59] M. Lim, H. Jaeger, Acoustically levitated lock and key grains, Bull. Am. Phys. Soc. (2022).